Hybrid PIC/Fluid Simulations of the Plume Expansion in a Magnetic Arch

IEPC-2024-472

Matteo Guaita[*] and Mario Merino[†] and Eduardo Ahedo[‡]
Department of Aerospace Engineering, Universidad Carlos III de Madrid, Leganés, Spain

Magnetic arches are an attractive option for the clustering of multiple electrodeless plasma thrusters, as they are characterized by a zero magnetic dipole moment and thus allow a reduction of the perturbing forces on the spacecraft. This work, therefore, employs the planar, hybrid code EP2PLUS to simulate the plasma expansion in this magnetic topology. First, a reference simulation is used to analyze the leading physical mechanisms that govern the plume's properties. Ions are thus found to be characterized by a double peaked VDF close to the symmetry plane, where the plasma beams emitted by the two thrusters merge, while the magnetic force acting on electrons is shown to shape both the lateral confinement of the plume, and the thrust profile provided. Secondly, a parametric sweep on the strength of the magnetic field shows that a saturation in the effects of the magnetic strength (both in the propulsive properties and in the characteristics of the plume) is observed for values of the Hall parameter larger than 10. Only the in-plane electron currents were found to be particularly sensitive both to the magnetization levels and to the boundary conditions employed, although they also resulted largely decoupled from the other plasma properties.

I.   Introduction

Electrodeless plasma thrusters (EPTs) are a rapidly emerging technology in the electric propulsion community because of their simplicity, scalability, and absence of plasma-immersed electrodes.[1,2] This family of thrusters most notably includes the helicon plasma thruster[3–5] and the electron-cyclotron resonance thruster,[6–8] in which the plasma generation is guaranteed by exciting the electron population through electromagnetic waves. A key component of these architectures is the magnetic nozzle (MN),[9–11] used to externally accelerate the plasma and increase the provided thrust. A traditional MN consists of a diverging magnetic field $\mathbf{B}$, applied by the thruster's magnetic circuit, which confines the plasma in the perpendicular direction and accelerates it axially. In fact, in the common case of an 'electron-pressure-driven' MN (where the electron temperature is much larger than the ions') the orthogonal electron pressure gradient, combined with the $\mathbf{E} \times \mathbf{B}$ drift, gives rise to an azimuthal and diamagnetic electron current $j_{\theta e}$. This generates a magnetic force density $-j_{\theta e} B_r$ that pushes electrons axially, and by reaction contributes relevantly to the total thrust provided by the EPT. To maintain a current free plume in the presence of the axial magnetic force acting on electrons, an ambipolar potential drop must also develop, confining electrons and generating an increase in axial momentum of ions equivalent to the magnetic thrust provided.[9,12]

A single MN produces a non-zero magnetic dipole moment that can give rise, in presence of terrestrial or planetary magnetic fields, to disruptive torques for the control of a spacecraft's attitude. However, with the aim of easily scaling the generated thrust and providing a form of thrust control, the idea of clustering multiple EPTs has been recurrently proposed in the literature.[13–16] It becomes therefore intuitive to envision the pairing of EPTs with opposite magnetic polarities, so as to cancel out the total dipole moment.[17] In such

---

[*]PhD student, EP2, mguaita@pa.uc3m.es.
[†]Permanent Professor, EP2, mario.merino@uc3m.es.
[‡]Permanent Professor, EP2, eahedo@ing.uc3m.es.

a configuration the gradually diverging magnetic topology of a MN is modified into a magnetic arch (MA), in which a portion of the magnetic field lines emitted by one of the EPTs curve and connect with those of the other.[13] These field lines are termed *closed magnetic lines*, while the outer lines of each EPT, which do not connect with those of the neighbouring one and close back on themselves are termed *open magnetic lines*. These definitions also allow to identify a separatrix, the magnetic line that lays on the boundary between open and closed lines, whose position and geometry (which also identifies the number of open and closed lines) depends on the details of the MA topology.

The magnetic topology of a MA implies important variations in the plasma response with respect to the traditional MN. Amongst these the most relevant are the coupling between the two plasma sources, which now result directly connected by the arching magnetic lines,[14] and the interaction and merging of the two plasma beams emitted by each EPT.[13] Additionally, in a MA the plasma must eventually move across some closed magnetic lines in order to expand downstream. While ions typically result unmagnetized because of their large mass, electrons must either move along the open magnetic lines present at the edges of the plume or undergo magnetic detachment from the closed ones to reach infinity[13] and grant a current-free plume. The failure to do so would eventually cause an electrostatic deceleration of ions and a reduction in the propulsive efficiency of the MA. This causes a design trade-off in the choice of the strength of the magnetic field. In fact, at lower magnetic flux densities the lateral confinement of the plasma decreases, and the propulsive force generated by the diamagnetic electron currents also drops. On the other hand, as the magnetic field is increased, electrons injected on one of the closed magnetic field lines will find it more and more complex to reach infinity, eventually decreasing the propulsive performance.

Although these differences with respect to traditional MNs are important, their investigation and treatment in the literature remains for the moment limited. Merino *et al.* explored for the first time an expansion in a MA by means of a planar, quasi-neutral, full-fluid approach, that considered perfectly magnetized and polytropic electrons and a single and cold ion fluid.[13] This allowed a first description of the general plasma and propulsive properties of a MA, highlighting the presence of a magnetic drag force in the region where the magnetic lines become perpendicular to the plasma flow, and the consequent importance of detachment in the propulsive performance. Indeed, it was found that a relevant role was played in this direction by the magnetic field induced by the electron currents in the plume, that caused an opening of the magnetic lines and an effective detachment of the plasma form the applied magnetic field. This model, however, also had important limitations in the physical description that it offered: electrons were assumed perfectly magnetized, collisional events were consequently fully neglected, and the ions were modelled by means of a single, cold fluid, mis-representing the complex double-peaked velocity distribution function (VDF) that develops at the intersection between the two plasma beams.

Later, Di Fede *et al.* investigated multiple architectures for EPT clusters by means of a 3D Particle in Cell (PIC) approach,[14] highlighting for the case of the MA the strong exchange of electron currents between the magnetically linked EPT sources. This was found to decrease the total electron current reaching infinity, and consequently reduced the total ambipolar potential drop that developed in the plume. Despite the relevance of this work, various open points were left pending: collisions were once again neglected, and no insight on the influence of the strength of the magnetic field on the plasma response was offered. Furthermore, other studies have suggested that in the case of magnetized plasmas a strong artificial scaling of the vacuum permittivity, such as the one employed in this work, may alter the plasma response and reduce the reliability of the results.[18,19]

Finally, a first experimental investigation of a MA was carried out by Boye *et al.*,[15] and proved the feasibility of the concept by detecting the flow of plasma across the closed magnetic lines as well as the theorized reduction of the plume divergence with respect to a MN configuration. This investigation also noted, in accordance with the previous numerical studies,[13,14] a reduction in the ion velocity in the far plume when the MA configuration was employed instead of two distinct MNs.

None of the publications mentioned so far have provided any insight into the effects of testing a MA inside experimental facilities, which in the case of MNs are responsible for relevant differences between the plasma response obtained in a vacuum chamber and in space. These effects are predominantly linked to the larger background pressure of neutral gas found in a testing facility, which can lead to: (i) the modification of the plasma density map, and an increase of the plume divergence due to resonant charge exchange (CEX) collisions between ions and neutrals,[20] (ii) an increased perceived mass flux due to the entrainment of ionized background neutrals in the plume expansion,[21–23] (iii) a reduction of the ion acceleration due to the electron cooling caused by inelastic collisions,[21,22] and (iv) an increased diffusion of electrons across magnetic lines

caused by collisional events.[24] Additionally, it has been suggested that the finite extension of the plume expansion permitted in a vacuum chamber, and the presence of conductive facility walls, may alter the map of electron currents[25] and in some cases strongly influence the value of the magnetic thrust provided by a MN.[26]

This work aims to investigate the open points identified in the literature with regards to the MA and its application for clusters of EPTs. Namely, we attempt here to further detail the physical processes governing the expansion of a MA plume, with particular attention on the interaction between the distinct plasma beams produced by each EPT, and the transport of plasma downstream across the closed magnetic lines. We then assess the influence of a variation in the magnetic field strength on the expansion properties, as well as facility effects linked to the vacuum chamber size and the collisional processes involving the neutral background population. For such a parametric study, a physically accurate, but computationally undemanding model was required. The 2D version of the in-house, hybrid code for plume simulations EP2PLUS was therefore employed, allowing a good compromise between the accuracy and the computational burden of simulations. The code has been presented, described, verified and validated in numerous previous publications. Amongst these we point to Reference 27 for a general overview of the code and a detailed description of the particle-wise algorithms and collisional operators, to References 28 and 29, respectively, for the derivation and numerical solution of the fluid equations for magnetized electrons, and to References 30 and 31 for examples of the verification and validation of the code.

The remainder of this article is structured as follows. The main characteristics of EP2PLUS and the modelling strategy are first explained in Section II. Then, Section IV describes a nominal simulation case, employed to showcase the general plasma response when expanding through a MA, and the resulting propulsive properties. An analysis of the effect of the magnetic field strength on the plume expansion is then presented in Section V, focusing on how its influence on the electron population translates into variations in the observed propulsive performance. Next, in Section VI we discuss the implications of the choice of boundary conditions (BCs) and domain size on the plume characteristics, examining also the effectiveness of the BCs introduced in our previous work in this more complex simulation scenario. Finally, a summary of the main conclusions of this work is carried out in Section VII.

II. Model

EP2PLUS simulates ions and neutrals through a particle in cell (PIC) description, and the electrons by means of a weakly-collisional drift-diffusion fluid model. At each time-step of the code, therefore, the heavy species and the electron modules are solved sequentially, with the former providing fundamental inputs to the latter through the hypotheses of a quasi-neutral and current-free plume. The computational loop is then restarted by advancing the heavy particles in the newly obtained electric field. The main features of the two modules are described in the following subsections.

A. Heavy Species Module

At each time-step ion and neutral macro-particles are advanced employing a standard series of PIC algorithms. Firstly, macro-particles are injected into the domain from appropriate injection surfaces. Secondly, a Boris-Cylrad Leapfrog scheme[32] is employed to integrate the particle's equation of motion according to the local electric and magnetic fields, linearly interpolated to the particle's position. Thirdly, MCC and DSMC collisional operators are applied to emulate inter-species interactions. Fourthly, boundary effects are evaluated for those particles that have crossed important surfaces (*i.e.* domain boundaries, or material walls). Finally, the macro-particles are weighed to the nodes of the structured mesh, through a tri-linear weighing scheme,[33] yielding the densities, fluxes and temperatures of each population. These are then passed as inputs to the fluid equation solver.

B. Electron Module

In the case of a quasi-neutral plasma, and for a quasi-stationary ($\frac{\partial}{\partial t} = 0$) and inertialess electron fluid, characterised by a diagonal and isotropic pressure tensor, the electric current continuity and the electron momentum equation respectively read

$$\nabla \cdot \mathbf{j} = 0, \tag{1}$$

and

$$-\nabla(nT_e) + en\nabla\phi + \mathbf{j}_e \times \mathbf{B} - \sum_{s=1}^{S} \nu_{es} m_e n(\mathbf{u}_e - \mathbf{u}_s) = 0. \tag{2}$$

Here most of the notation is standard, so that $n = n_i = n_e$ represents the quasi-neutral plasma density, $\mathbf{j} = \mathbf{j}_i + \mathbf{j}_e$ indicates the total electric current density obtained as the sum of the ion and electron currents, $\mathbf{u}_e = -\boldsymbol{j}_e/en$ the bulk velocity of the electron fluid, and T_e the scalar electron temperature in energy units. Moreover, e is the elementary charge, ϕ the electric potential, $\mathbf{B}$ the applied magnetic field vector, and m_e the electron mass. Finally, the suffix s is used to discern between quantities relative to the different heavy species present in the simulation, so that ν_{es} is the collision frequency between electrons and the heavy species s, and $\mathbf{u}_s$ is the bulk velocity of the species' distribution function.

In the version of EP2PLUS used here, the electron fluid equations are closed at the level of the momentum through the polytropic law

$$T_e = T_{e0} \left(\frac{n}{n_0}\right)^{\gamma-1}. \tag{3}$$

where both the polytropic coefficient γ and the constants T_{e0} and n_0 are calibrated empirically.

The polytropic law allows to define a thermalized potential[34]

$$\Phi = \phi + \frac{\gamma}{e(\gamma-1)} T_{e0} \left[1 - \left(\frac{n}{n_0}\right)^{\gamma-1}\right], \tag{4}$$

such that the 'generalized electric force' $en_e\nabla\Phi$ groups the pressure and electric forces on electrons. Numerically, solving the fluid equations in terms of the thermalized potential results advantageous, as it allows to reduce numerical cancellation errors[35] between these two counter-acting forces. By now introducing a total electron momentum transfer collision frequency $\nu_e = \sum_s \nu_{es}$; an equivalent current density $\mathbf{j}_c = (en/\nu_e) \sum_s \nu_{es}\mathbf{u}_s$ that groups all collisional effects from the heavy species; the electron scalar conductivity $\sigma_e = e^2 n/(m_e\nu_e)$; and the Hall parameter $\chi = eB/(m_e\nu_e)$; the electron momentum equation can be solved for the total electric current density, yielding the generalized Ohm's law[28]

$$\mathbf{j} = -\mathcal{K} \cdot (\sigma_e\nabla\Phi + \mathbf{j}_c) + \mathbf{j}_i. \tag{5}$$

Where, if written in a reference frame $\{\mathbf{1}_\parallel, \mathbf{1}_\perp, \mathbf{1}_y\}$ aligned with the magnetic field,

$$\mathcal{K} = \frac{1}{1+\chi^2} \begin{bmatrix} 1+\chi^2 & 0 & 0 \\ 0 & 1 & -\chi \\ 0 & \chi & 1 \end{bmatrix} \tag{6}$$

is the normalized conductivity tensor. Of course, in the practical implementation of the code, this conductivity tensor must be appropriately rotated to the general Cartesian frame $\{\mathbf{1}_x, \mathbf{1}_y, \mathbf{1}_z\}$ employed.

Once the appropriate boundary conditions are provided (see Section III) the system of Eqs. (1) and (5) is solved for $\mathbf{j}_e$ and Φ with the staggered Finite Volume scheme presented in Reference 29. The new potential map, required to further advance the ion macro-particles, is then retrieved through Eq. (4).

III. Simulation Setup

As mentioned, the simulations presented in this work are structured so as to reproduce the problem analyzed in Reference 13. The present Section therefore defines the reference scenario initially employed to analyze the general plasma response in the study case of interest. This case will then be generalized and expanded in the following Sections but, unless otherwise stated, most properties and simulation settings described hereafter will remain unchanged.

The domain under investigation is defined by a right-handed reference frame with a Cartesian vector basis $\{\mathbf{1}_x, \mathbf{1}_y, \mathbf{1}_z\}$, oriented so that the Oxz plane coincides with the 2D expansion plane, and the Oz axis points downstream. As a result, the Oy axis lies on the out-of-plane direction of the 2D expansion, along which the plasma properties are assumed infinitely uniform. Two plasma sources, emitting along $\mathbf{1}_z$, are located on the Oxy plane and span respectively from $x = -6\,\text{cm}$ to $x = -4\,\text{cm}$ and from $x = 4\,\text{cm}$ to $x = 6\,\text{cm}$, so
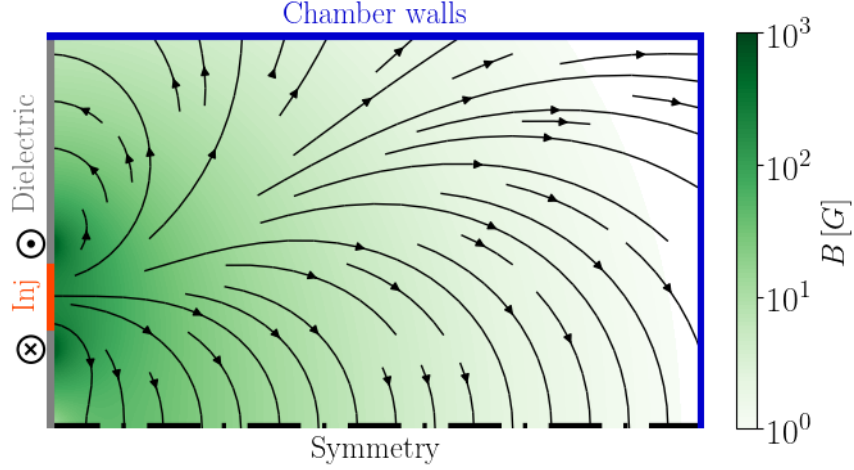
Figure 1: Sketch of the simulation domain and of the boundary conditions applied. The green color-map and the streamlines display the intensity and direction of the magnetic field for the reference case.

that Oyz represents the simulations' symmetry plane. The applied magnetic field $\mathbf{B}$ is generated by four infinite electric wires positioned respectively in $x = $ -7, -3, 3, 7 cm, and $z = 0$, each carrying the same electric current I along $\mathbf{1}_y$. The signs of the electric currents flowing along the wires are anti-symmetric about the Oyz plane, so that the total magnetic moment of the system is null, and the magnetic field at the center of each source is of $B_0 = 300$ G. Figure 1 shows a sketch of the considered magnetic topology and simulation domain, which corresponds to half of the physical domain described thanks to symmetry conditions.

For this reference case no population of neutral particles is considered in the simulation. In fact, we find that it aids the discussion to first analyse the plasma response in the case of a simplified physical scenario, where the complexity of the numerous collisional processes that take place in a plasma plume is reduced. We prefer, therefore, to employ the adimensional Hall parameter χ as a free parameter of the model. This also allows a clearer and more direct parametric analysis of magnetization effects on the plume properties, carried out in Section V. In the reference simulation presented here, therefore, an arbitrary and uniform value of $\chi = 30$ is imposed over the whole domain, ensuring a strong magnetization of the electron fluid and thus an effective working regime for the MA. Consequently, the electron scalar conductivity is accordingly locally adjusted as $\sigma_e = en\chi/B$. This simplification also requires a further assumption to be made on the value of $\mathbf{j}_c$, which cannot be self-consistently computed in absence of a neutral population. However, because of the large values assumed by the electron conductivity in typical plasma plumes ($\sigma_e = \mathcal{O}(10^2)\mathrm{AV}^{-1}\mathrm{m}^{-1}$), the contribution of $\mathbf{j}_c$ in Equation 5 can be safely neglected with respect to that of the term $\sigma_e\nabla\Phi$.[27]

Finally, regarding the electron polytropic closure, the reference point is fixed at the center of the injection surface ($x_0 = $5 cm, $z_0 = 0$), the reference plasma density and electron temperature are $n_0 = 10^{18}\mathrm{m}^{-3}$ and $T_{e0} = $5 eV, and a polytropic coefficient $\gamma = 1.2$ is employed.[36,37]

A. Domain Boundaries

As mentioned, the solution of the electron fluid Eqs. (1) and (5), requires the imposition of boundary conditions on all of the domain edges. Here the unknowns of the system are the thermalized potential (which replaces the more physical but numerically less stable electric potential) and the electron currents. The BCs can therefore be applied either on the value of Φ (Dirichlet conditions) or, more commonly, on the local normal electric current density $j_n = \mathbf{j}\cdot\mathbf{1}_n$ (Neumann conditions), with $\mathbf{1}_n$ the outward versor normal to the boundary. Additionally, particles crossing any domain boundary must also be correctly treated depending on the boundary type. Figure 1 details the type of boundaries employed in this work, and the consequent BCs imposed on the electron fluid and on the particle populations are described in the following subsections.

1. Symmetry Boundary

In order to impose symmetry conditions, a null perpendicular current ($j_n = 0$) is imposed as BC for the fluid equations, while all particles crossing such boundaries are specularly reflected. Note that under these conditions $j_{ni} = j_{ne} = j_{nc} = 0$, so that Eq. (5) yields $\nabla \Phi \cdot \mathbf{1}_n = 0$ as expected on a symmetry plane.

2. Injection Boundary

The plasma injected into the domain by the EPT source is composed of singly charged Xenon ions and electrons. The ion particles are injected by sampling through an acceptance-rejection algorithm[38] the forward portion of a Maxwellian distribution function.[27] This Maxwellian VDF is characterized by a Gaussian density profile centered in $x_0 = 5\,\mathrm{cm}$, a uniform temperature profile, and a sonic velocity $c_s = \sqrt{\gamma(T_e + T_i)/m_i}$:

$$n_{i0}(x,0) = n_0\, 10^{-3[2(x-x_0)/L]^2}, \tag{7}$$

$$\mathbf{u}_{i0}(x,0) = c_s(x,0)\mathbf{1}_z, \tag{8}$$

$$T_{i0}(x,0) = 0.1\,eV. \tag{9}$$

Note that, with these injection conditions, ions at the center of the injection surface have an average Larmor radius $r_{li} = m_i u_{i0}(x_0,0)/(eB_0) = 1.5\,\mathrm{cm}$. Taking the width of the injection surface ($L = 2cm$) as a characteristic dimension of our problem, ions result initially mildly magnetized and are expected to rapidly demagnetize as the intensity of the magnetic field drops and they are accelerated downstream. Finally, any particle returning to the injection surface from inside of the domain is simply removed from the simulation.

Regarding the electron fluid, instead, it is assumed that in the quasi-neutral bulk of the EPT source an equilibrium between the lateral electron pressure and magnetic forces exists. This, through Eqs. (2) and (4), yields a flat electric potential profile, and an inverted Gaussian profile to be imposed as Dirichelet BCs for the thermalized potential

$$\phi_0(x,0) = 0, \tag{10}$$

$$\Phi_0(x,0) = \frac{\gamma}{e(\gamma-1)}T_{e0}\left[1 - 10^{-12(\gamma-1)[(x-x_0)/L]^2}\right]. \tag{11}$$

3. Dielectric Boundary

A dielectric condition is imposed along all of the upstream boundary, with the exception of the injection region. Since a neutral particle population is omitted, and therefore ion recombination at material walls can be neglected, all particles crossing this surface are removed form the simulation. From the point of view of the electron fluid, a Neumann condition is imposed on Φ by locally requiring that $j_{ne} = -j_{ni}$, with the latter value of the normal ion current obtained from the heavy species module.

4. Chamber walls

In the commonly adopted experimental scenario in which the vacuum-chamber and the thruster body are electrically decoupled (i.e. a floating thruster configuration) a zero net current flowing to the facility walls should be obtained at steady-state. In order to enforce this condition, let ϕ_W be the potential of the metallic chamber, and let us call Q the local edge of the Debye sheath that develops between the quasi-neutral boundary of the domain and the facility walls. The sheath is assumed electron-confining, planar, collisionless, and characterized by an undrifting Maxwellian electron distribution. Then, according to classical sheath theory, the electron current density crossing locally the sheath is[39]

$$j_{neQ} = -e\left[n\exp\left(\frac{e(\phi_W - \phi)}{T_e}\right)\sqrt{\frac{T_e}{2\pi m_e}}\right]_Q, \tag{12}$$

and imposing that the total electric current collected by the facility walls is zero one has

$$I_{iW} + \int_{A_{out}} j_{neQ}(\phi_W)dA = 0. \tag{13}$$

With I_{iW} the total ion current flowing towards the wall, computed from the heavy species module. This equation is implicit for the facility potential ϕ_W, and is therefore solved with an iterative Newton-Raphson scheme at each time-step. Once ϕ_W is known, Eq. (12) provides the boundary condition for the electron current density to be imposed in the electron module.

Regarding the heavy species, all particles crossing these boundaries are removed from the simulation, analogously to what is done in the case of the dielectric boundaries.

B. Numerical settings

The rectangular domain of Figure 1 of size $L_x \times L_z$ is discretized by means of a uniform mesh composed of 180×300 cells of dimensions $\Delta x \times \Delta z$. Moreover, to guarantee the stability of the model the simulation time-step is required to respect a CFL-like condition $\Delta t < \Delta z / u_{i0}$.[33] Finally, the simulation was considered at steady state after a simulation time of $t_{ss} = 2L_z/u_{i0}$. This was confirmed by verifying that both the number of macro-particles in the domain, and the value of the facility potential ϕ_W varied by less than 1% over the last 700 steps. The most relevant simulation settings for the reference case are summarized in Table 1.

Parameter	Value	Parameter	Value
L_x	15 cm	Δx	$0.8\bar{3}$ mm
L_z	25 cm	Δz	$0.8\bar{3}$ mm
t_{ss}	500 μs	Δt	7×10^{-2} μs
n_0	10^{18} m^{-3}	T_{e0}	5 eV
χ	30	γ	1.2

Table 1: Summary of the most relevant settings for the reference simulation case.

IV. The Reference Simulation

The Panels of Figure 2 show the steady-state maps for the thermalized potential Φ, electric potential ϕ, plasma density n and in-plane ion velocity $\tilde{\mathbf{u}}_i$. To aid with the ensuing discussion, Figure 3 also displays the profiles of Φ, ϕ and n along the symmetry boundary of the simulation ($x = 0$) and the axis $x = 5$ cm of one of the injection surfaces. Figure 4, instead, presents the same plasma properties at axial sections with $z = 0, 10, 20$ cm. The values corresponding to the reference simulation analysed here are marked with green squares in the two latter plots. The analysis of the steady-state properties of a strongly magnetized plasma expansion ($\chi \gtrsim 10$) is most easily tackled by starting from the map of the thermalized potential. Indeed, as we will further discuss later, for large values of the Hall parameter the thermalized potential Φ remains roughly constant along the magnetic lines. This can be ascertained by observing the magnetic lines overlain in white in Figure 2(a). As a consequence, in this regime, the value of Φ in the domain is mostly dependant on the chosen boundary conditions, and is decoupled from the remaining plasma properties. The inverted Gaussian profile of Φ imposed at the injection surface through Eq.(11) (see Figure 4(a)) is in fact mapped over the whole simulation domain by following the magnetic field lines, forming the curved valley observed in the 2D profile of Φ. A given profile of the thermalised potential imposes a strict relationship between the electric potential and the ion density through Eq. (4), which together with the ions' equation of motion determines the maps of ϕ, n and $\tilde{\mathbf{u}}_i$.

The two lobes of high electric potential at the edges of the injection surface in Figure 2(b), together with the sharp axial decrease immediately in front of it (see also Figure 3(d)) force ions to initially accelerate axially, following the magnetized electron fluid. As the magnetic lines begin to diverge, however, so does the plasma beam, although the large inertia of ions, which in this point in the domain already result largely unmagnetized, allows a slight diffusion of the plasma density across the field lines (see Figure 2(c)). This is evidenced by the relative angles between the velocity streamlines and the magnetic field lines in Figure 2(d). The strong initial axial acceleration combined with the outward curving of the magnetic lines, in fact, causes ions to detach inwards as they advance downstream. This portion of the domain is the *near-plume*, in
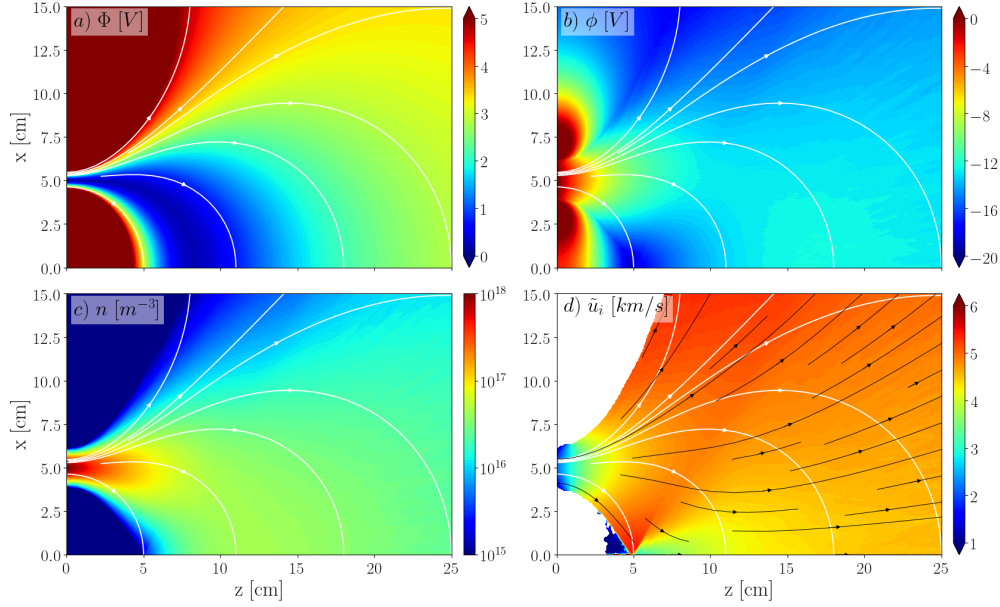
Figure 2: Plasma properties in the reference case.

which the two ion beams proceeding from the distinct plasma sources are yet to interact, and the expansion in front of each EPT is independent of the other. As a consequence, the plume's behaviour here is analogous to the one observed for a traditional MN, which is typically characterized by an inward ion detachment and a strong axial drop in the plasma density and electric potential[9] (see the right column of Figure 3).

Starting from $z \approx 6$ cm, however, the ion beam begins to merge at the symmetry plane with the one emitted from the specular source (here represented by macro particles reflected at $x = 0$). As a result the ion density, along with the thermalized and electric potential, rises when moving downstream along the symmetry axis (see the first column of Figure 3). In the lateral direction, on the other hand, these quantities do not display a single peaked profile yet (see the second column of Figure 4), indicating that the coalescence of the beams is still under way. The plume's behaviour thus drifts away from the one of a MN, signaling the entrance into the *transition-region*. Here, the magnetic lines begin to curve back towards the symmetry plane to close into the specular EPT source, and Figure 2(d) shows that the majority of ion streamlines are now forced to detach outwards in order to continue their axial motion downstream. Nevertheless, a region of inwards detachment persists beyond the magnetic separatrix dividing open and closed field lines in the top left portion of the domain.

As the ion beams begin to merge at $z \approx 6\,cm$, the radial velocity of the total ion population reduces to zero near the lower edge of the simulation domain. This results in the sharp drop observed in Figure 2(d) in the magnitude of the ion velocity and the swift axial swerve of their streamlines around $x = 0$, $z \approx 6$ cm. Note that, conversely to what is observed in traditional MN geometries or unmagnetized plumes, the axial potential profile from this point downstream increases rather than dropping, as highlighted by Figure 3(c). Consequently, the ions moving downstream along the symmetry axis experience a slight deceleration. This is caused by two concurring effects. The first is the closed magnetic topology of the MA, characterized by magnetic lines orthogonal to the axial direction in the proximity of the symmetry plane, which have the effect of reducing the axial mobility of electrons. To maintain quasi-neutrality, therefore, the axial force acting on ions must also decrease. The second is the symmetrical geometry of the problem, which causes a rise in the plasma density where the ion beams meet (see Figure 3(e)). Under the polytropic assumption this also implies an additional confining contribution of the pressure forces acting on the electron fluid, which must again be balanced by the electric field. Mathematically this effect is obtained by the inversion and axial derivation of Eq. (4) to yield the axial electric field

$$E_z = -\frac{\partial \Phi}{\partial z} - \gamma \frac{T_{e0}}{en_0} \left(\frac{n}{n_0}\right)^{\gamma-2} \frac{\partial n}{\partial z}. \tag{14}$$
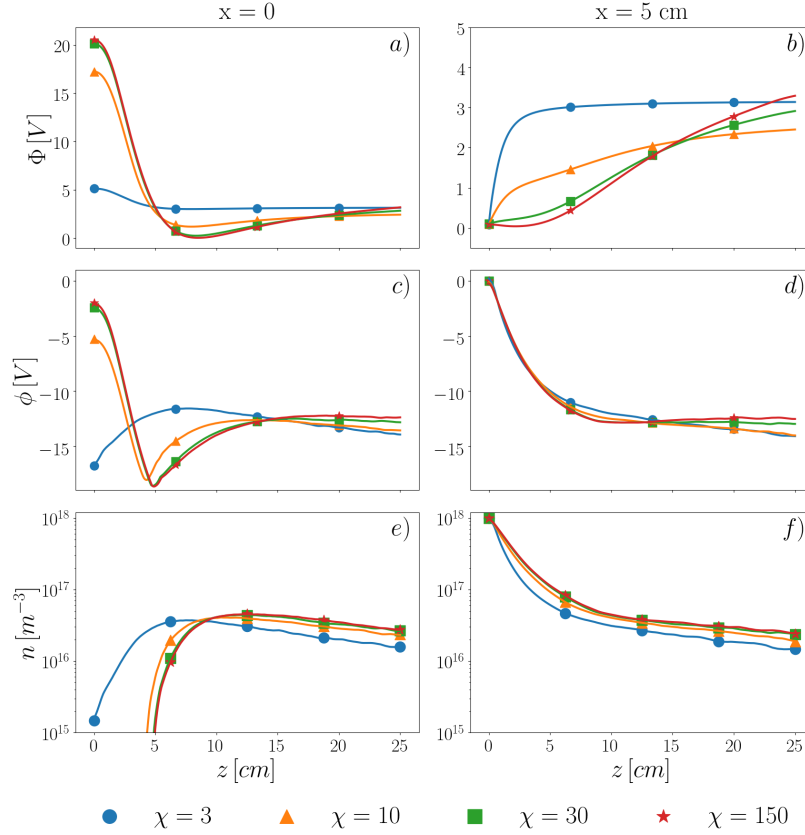
Figure 3: Comparison of the axial profiles of Φ, ϕ, and n for all simulation cases. The first column of plots shows the plasma properties along the symmetry plane, the second along the axis of the plasma source. Note the changes in scales in the y axes between the first and second columns of plots.

While in most conventional plumes the second term in this equation provides a positive contribution as the plasma expands, in this case it can have a negative effect due to the increase in density observed along the symmetry plane. Likewise, the axial profile of the thermalized potential displays an initial sharp drop followed by a gradual axial increase due to the mapping of the injection BCs to the points of the symmetry plane (refer to Figure 3(a)). It is this later, gradual rise in Φ that, together with the corresponding increase in the plasma density, causes negative values of E_z and a deceleration of the ion population. It is interesting that, although at the outer edges of the plume the ions continue to accelerate downstream, the effect just described acts on the denser portion of the plasma bulk and on the axial component of the ion momentum, and therefore has, as will be seen later, a negative impact on the provided thrust.

Starting from the local maximum in the plasma density along the symmetry plane (at $x = 0$, $z \approx 12.5\,cm$) the two plasma beams can be considered fully merged into a unique *far-plume*, and all properties present single-peaked profiles along x (see the right-most Panels of Figure 4). At the outer edges of the plume the ion streamlines continue to diffuse outwards across the field lines, similarly to what happens in a MN. At the center, instead, the magnetic lines become roughly parallel to the x axis, forcing the ions to cross them orthogonally in order to expand downstream. Soon, however, the magnetic and electric forces acting on the ions become small enough to be neglected, and their streamlines result essentially straight.

The differentiation of the thermalized potential map allows, through Eq. (5), the retrieval of the in-plane and out-of-plane electron current densities ($\tilde{\jmath}_e$ and j_{ye} respectively). These are displayed in Figure 5, together with the in-plane total current density $\tilde{\jmath} = \tilde{\jmath}_i - \tilde{\jmath}_e$. Note that, considering the conductivity matrix written in a magnetically aligned reference frame in Eq. (6), and keeping in mind that all out-of-plane gradients are null, the out-of-plane currents result a factor χ larger than the in-plane ones. This is confirmed when comparing the scales of Panels (a) and (b). Indeed, the first panel displays a large diamagnetic loop of
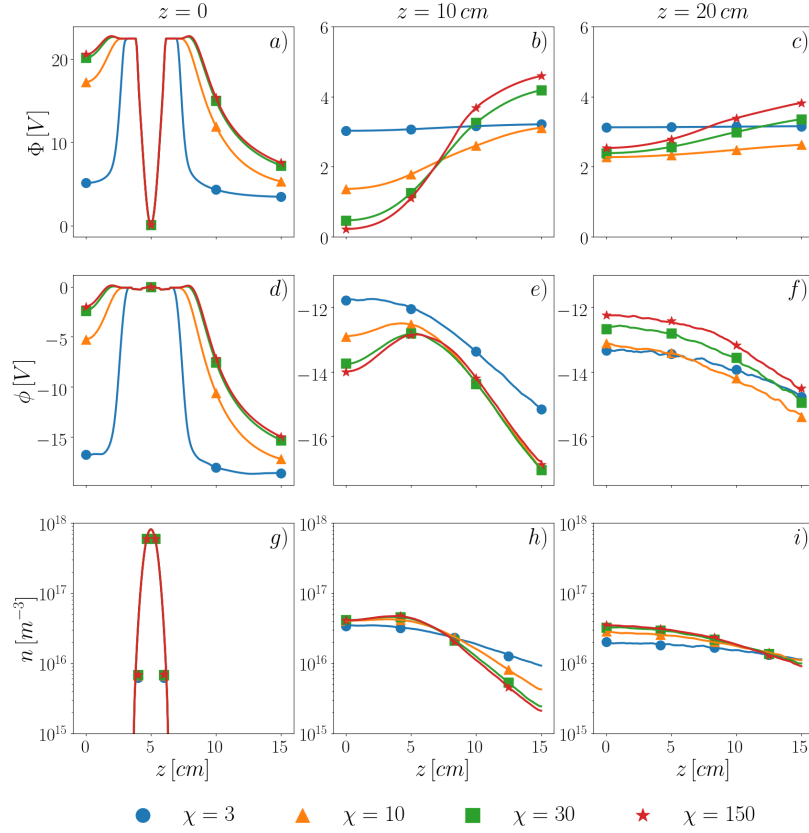
Figure 4: Comparison of the lateral profiles of Φ, ϕ, and n for all simulation cases. The first column of plots shows the plasma properties at the injection surface, the second and third at $z = 10, 20\,cm$. Note the changes in scales in the y axes between the first column of plots and the other two.

electron currents (exiting the simulation plane in the bottom, red part of the plot, and entering it in the upper, blue portion), which, because of the negligible ion velocities in the out-of-plane direction, can be considered equal to the total out-of-plane current density $j_y = j_{ye} + j_{yi} \simeq j_{ye}$. Note that the curvature of the axis of the diamagnetic current loop (easily identifiable by the line $j_{ye} = 0$), turns towards the symmetry plane so that it is always aligned with the externally imposed magnetic field. This generates the in-plane magnetic forces which are fundamental for the lateral confinement of the plasma plume and, as will be discussed shortly, for the propulsive performance of a MA.

Figure 5(b), on the other hand, shows clearly that the value of the Hall parameter $\chi = 30$ considered here is insufficient to force the electron current to precisely follow the magnetic lines. Indeed, numerous electron streamlines move across to the magnetic field to reach the downstream domain boundary. Nevertheless, the effect of magnetization may be appreciated by noting that the magnetic lines that lead to the domain corners (highlighted in the plots by the thicker white lines) carry larger current values with respect to the ones found in their surroundings. This is due to the larger mobility of electrons moving along magnetic lines rather than across them, and to the presence of the symmetry plane, that imposes a null outflow of currents through the bottom domain boundary. As a consequence, slightly reduced values of the electron currents are observed in the roughly semi-circular region of space below the magnetic line to the bottom corner, where electrons must diffuse across the magnetic field to leave the domain. The flow of electron currents results instead more free in the upper portion of the domain, where electrons can run along the magnetic lines to reach the downstream boundaries. In particular the two magnetic lines that reach the domain corners result particularly effective for the outflow of electrons, since they approach the domain edges asymptotically and therefore encompass a larger effective outflow area with respect to other magnetic lines. This effect is even more prominent in the plot of the total current density. A noticeable current arc
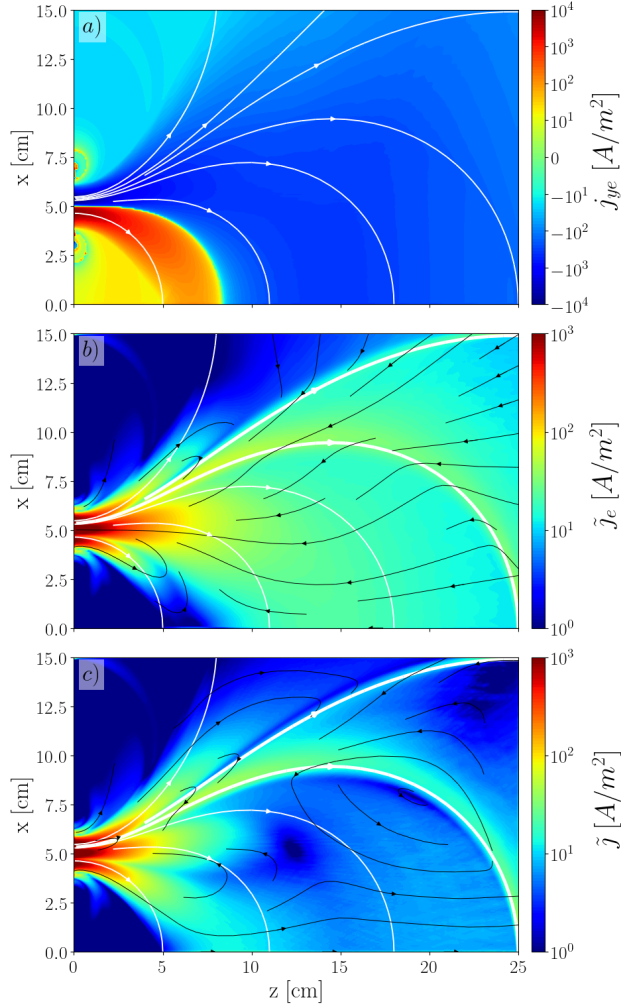
Figure 5: The in-plane electron and total currents (Panels (a) and (b)), and the out-of-plane electron currents (Panel (c)).

forms, in fact, around the magnetic line that passes through the bottom right corner of the domain. Indeed, the increased mobility of electrons flowing parallel to the magnetic field above it has the effect of shifting the electron flux imperceptibly towards bigger values of x, and causes the backstreaming total currents observed above this magnetic line. Below it, on the other hand, current flows mainly downstream, indicating a larger ion axial current -uninfluenced by the magnetic field and therefore flowing straight in the axial direction-, than the negative electron one. Finally, it is important to mention that, in the weakly collisional regime of interest, the solution for the in-plane electron currents results strongly decoupled from the general response of the plume. In fact, even large changes in the value of $\tilde{j}_e$ in Eq. (5) will only lead to marginal changes in the map of Φ (and consequently in the other plasma properties), because of the vary large values typically assumed by σ_e.

As mentioned, the out-of-plane diamagnetic currents ultimately provide the magnetic force crucial for the propulsive performance of magnetic nozzles. Indeed, the accumulated axial magnetic thrust (per unit of y-length), $F_m(z)$ generated in a control area Ω by a planar MA is

$$F_m = \int_\Omega -j_y B_x \, d\Omega. \tag{15}$$

Taking $\Omega(z)$ corresponding to the portion of the domain spanning from $z = 0$ to a given z coordinate, Figure 6 plots the accumulated magnetic thrust thus computed, expressed as a fraction of the thrust produced by the EPTs in absence of a MA ($F_0 = 12.5mN/m$). Once again the results obtained for the reference case

described here are marked with green squares. The magnetic propulsive force displays an initial sharp rise, corresponding to the first portion of the plume where the magnetic field vector is predominantly directed axially and the intensity of j_{ye} is largest. As the field lines bend in the lateral direction, however, the total magnetic thrust provided drops slightly, showcasing the resistance of the magnetic field to the axial expansion of the plasma plume. This is a natural consequence of the closed topology of a MA, and is also highlighted by the deceleration of the ion population close to the symmetry axis discussed above. Indeed the axial coordinate at which we observed the decrease in the ion velocity corresponds roughly to the one of the maximum cumulative magnetic thrust. These observations highlight the necessity of plasma detachment in the far plume of a MA, to avoid the null total magnetic thrust that would ensue from a magnetic resistance that extends to infinity.
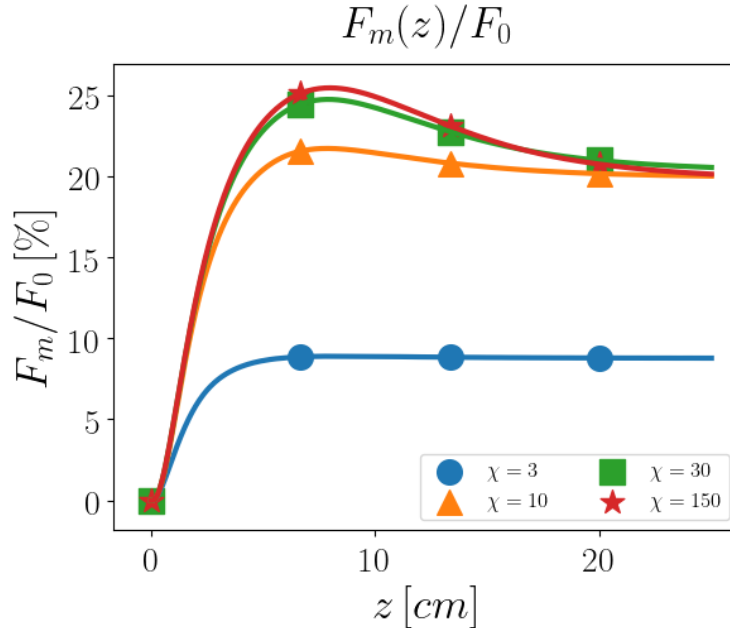

$$F_m(z)/F_0$$

Figure 6: Comparison between the accumulated axial magnetic thrust for all simulations, expressed as a percentage of the thrust obtained by EPTs with no MA $F_0 = 12.5 \, \mathrm{mN/m}$.

It is important to mention that the results obtained in Reference 13 for a simulation case analogous to the one presented here displayed in all ion properties a shock-like structure that propagated from the symmetry plane. The main difference between that work and the present one is, indeed, the model adopted for the ion population, which is here described through the PIC approach as opposed to the single fluid formulation employed there. By simulating the ions with a kinetic approach, the formation of a double-peaked ion VDF is observed in the region close to the symmetry plane, where the two ion beamlets deriving from the distinct plasma sources merge. Each peak of the VDF represents the ions pertaining to one of the two sources. Indeed, Figure 7 displays the ion VDF measured at $x = 0$, $z = 6 \, \mathrm{cm}$, which presents two marked and symmetrical peaks at energies corresponding roughly to the potential drop that develops between the injection surface and the considered location $\Delta\phi \approx 20 \, \mathrm{V}$. Although, taken individually, each ion beam only has a temperature of $0.25 \, \mathrm{eV}$ and can be roughly considered to be mono-energetic, their coalescence results in a VDF with a spread in velocities corresponding to a temperature $T_i \approx T_{e0} = 5 \, \mathrm{eV}$. Such a distribution cannot be represented with a single and cold ion fluid as done in Reference 13, causing the shock-like artefact observed in that work.

V.   The Effect of the Magnetic Field Strength

Having presented and analysed the general properties of a plasma expanding through the magnetic topology of a MA, we now investigate how this response is influenced by the strength of the applied magnetic field. We therefore consider three additional cases, identical to the reference one except for the intensity of
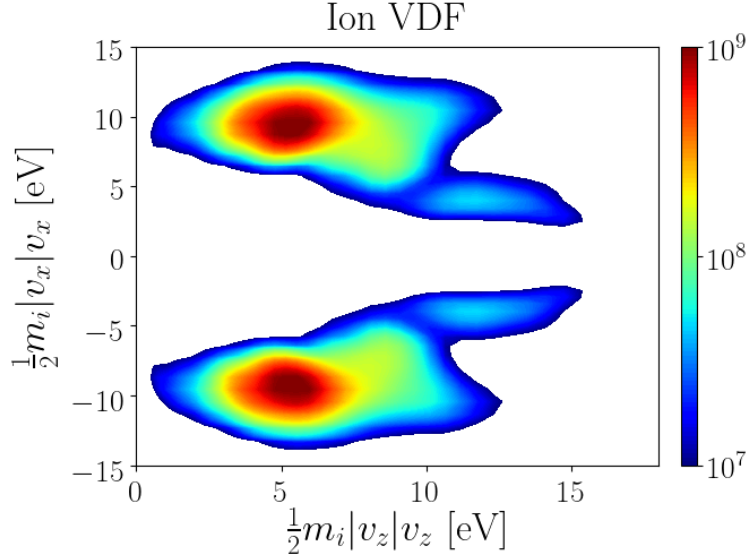
Figure 7: Ion VDF at $x = 0$ and $z = 6\,\mathrm{cm}$

the magnetic field map, which is modulated to yield $B_0 = 30, 100$, and $1500\,G$ at the center of the injection surface. Under the assumption that the electron collision frequency ν_e remains unvaried between simulations, the Hall parameter is also proportionally scaled to $\chi = 3, 10$, and 150. Figures 3 and 4, along with Figure 6, already displayed the axial and lateral profiles of the plasma properties and magnetic thrust obtained for these new values of χ. It results immediately evident that the cases with $\chi = 10, 30$ and $\chi = 150$ yield very similar results, and the Hall parameter has to be decreased to $\chi = 3$ for relevant changes to develop. In fact, the value of χ affects the employed electron model only through the conductivity tensor introduced in Eq. (5). As the Hall parameter increases, the conductivity tensor has the effect of decoupling the electron currents perpendicular to the magnetic field from the gradients of Φ through a factor $1/(\chi^2 + 1)$. This essentially inhibits the diffusion of electrons perpendicular to the magnetic field, and confines their motion along the magnetic lines, impeding the lateral expansion of the plume under the effect of the electron pressure gradients. The magnitudes of $\tilde{j}_e$, however, are delimited throughout the domain by the BCs employed and the continuity equation. As a consequence, because of the large values of σ_e that characterize the weakly collisional plasma typical of a MA, the parallel gradients of Φ must result negligible in order to produce finite electron currents along the magnetic lines. As we approach the case of perfect magnetization and an infinite Hall parameter, then, the thermalized potential must remain constant along the magnetic lines, so that it's map in the domain will only depend on the values imposed at the injection surface and on the magnetic topology. As a consequence, for values of χ higher than 10 only small variations will be observed in the map of Φ, and in the general plasma response. Keeping this in mind, and for the sake of conciseness, the present section employs mainly the comparison between the cases with $\chi = 3$ and $\chi = 150$ to showcase the effects linked to variations in the electron magnetization.

Figure 8 compares the general plasma properties obtained with $\chi = 3$ and $\chi = 150$. The first thing that jumps to the eye is the noticeable differences between the maps of the thermalized potential. As for the reference case, in the case with $\chi = 150$ the profile of Φ imposed at the injection surface remains practically constant along the magnetic field lines, and is mapped over the domain by following them, in accordance to what is expected in a strongly magnetized plasma. On the other hand, when $\chi = 3$ the electron currents may more freely move across the magnetic lines, allowing larger currents to form in the domain and then close at domain boundaries which would have previously been shielded by the magnetic field. Steeper gradients of Φ can therefore form along the magnetic lines, and the inverted Gaussian profile of Φ imposed at injection through Eq. (11) gradually dissipates along the domain (see Figures 3(b) and 4(b)). This parallel smoothing of the gradients of Φ also allows a reduction of the cross field gradients of the thermalized potential, so that the map of Φ in the far plume results nearly uniform and flat.

The first effect that the larger cross-field mobility of electrons obtained for $\chi = 3$ has on the map of ϕ
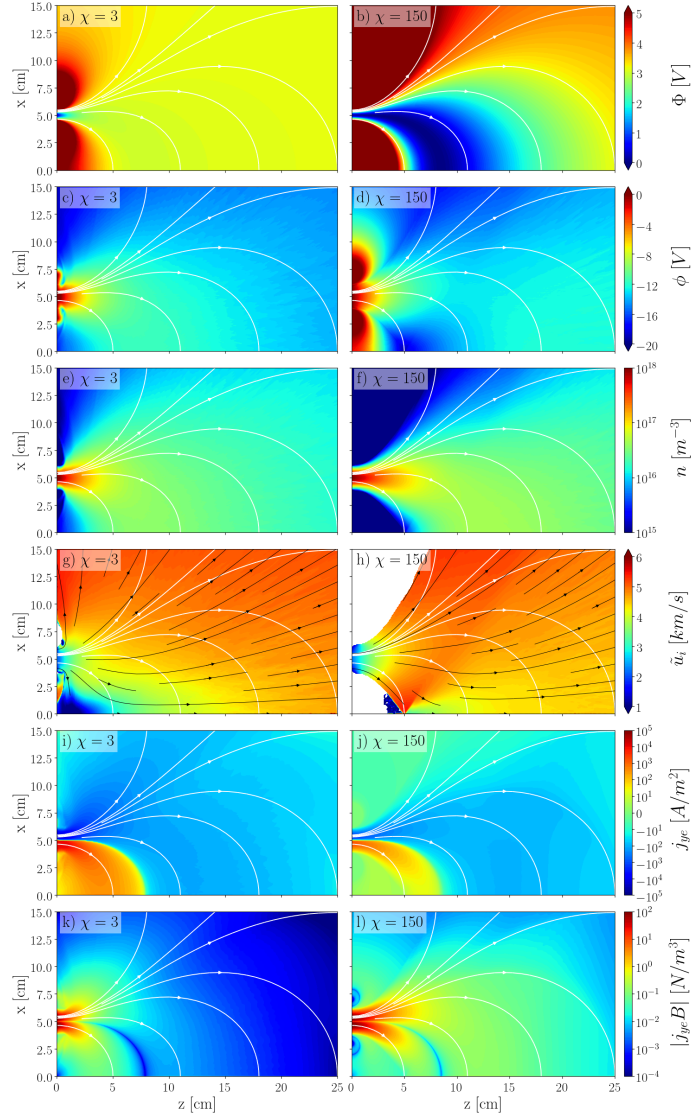
Figure 8: Comparison of the main plasma properties for $\chi = 3$ and $\chi = 150$.

is the relevant reduction of the two lobes of high electric potential at the edges of the injection boundary, caused by the decay of the lateral gradients of Φ. These lobes, as already commented in Section IV, had the effect of laterally confining the ion beam in order to follow the magnetized electron fluid. As a result, both the maps of the plasma density and ion velocity depict a less dense and more divergent plume for the case with $\chi = 3$ than with $\chi = 150$. Secondly, the potential rise that was observed in the reference case after the merging of the ion beams is present and enhanced for $\chi = 150$, but is instead shifted upstream and flattened out when lowering the Hall parameter to 3 (see the first column of Figure 3). In fact, although the axial increase in density along the symmetry plane is still present in both simulations, it moves upstream for the less magnetized and focused plume. Moreover, the axial rise in the thermalized potential observed in the more magnetized cases from $z = 8$ cm downstream, and which contributed to the negative axial electric field in this region of the domain, is absent for the case with $\chi = 3$ because of the smoothing of the map of Φ obtained at low magnetic fields. Observing the map of the ion velocity, this results in a monotonic axial acceleration of ions along the symmetry axis of the domain for $\chi = 3$, and a more complex profile for $\chi = 150$. In this latter case, in fact, ions are strongly accelerated by the sharp potential drop present just in front of the plasma injection, but are then mildly slowed down close to the symmetry plane (note the axial potential rise after $z = 5$ cm in Figure 3(c)). The result is that at the downstream boundary of the

domain ions have roughly reached the same outflow velocity for both cases, and noticeable variations in the ion velocity are only observed at the upper simulation boundary.

The last Panels of Figure 8 show the out-of-plane electron currents, and the corresponding magnetic force density $j_{ye}B$ responsible for the magnetic thrust and the lateral confinement of the plume. It is interesting to note here that the magnitude of j_{ye} displays a non-monotonic variation as the strength of the magnetic field increases. Between $\chi = 3$ and $\chi \approx 10$, in fact, the plume undergoes a noticeable magnetic focusing under the effect of the rising magnetic force, causing the reduction the lateral expansion and an increase the densities in the plume bulk. These larger densities and the smaller divergence of the plume are responsible for the increase in the magnitude of j_{ye} observed between Figure 8(i) and Figure 5(c). As the strength of the magnetic field further increases, however, the plume does not display further focusing, since the density isolines already roughly correspond to the magnetic field lines. The confining magnetic force $j_{ye}B$ necessary to balance the expanding action of the electron pressure (shown in Figure 8(l)) is therefore roughly constant for $\chi > 10$, and can be obtained with smaller out-of-plane currents as B increases. The magnitude of j_{ye} is therefore observed to decrease as χ moves from 30 to 150 (see Figures 5(c) and 8(j)).

	η_{div} [%]	ϕ_W [V]
$\chi = 3$	68.6	-21.96
$\chi = 10$	78.4	-22.92
$\chi = 30$	80.6	-22.75
$\chi = 150$	80.9	-22.55

Table 2: Divergence efficiencies and values of the facility potential for the different simulations considered.

Nevertheless, because of the higher plasma densities found at the symmetry plane for larger values of χ, the propulsive performance of the MA is expected to increase as the strength of the magnetic field rises. Table 2, in fact, shows how the divergence efficiency of the plume η_{div}, obtained as the ratio between the flux of axial kinetic energy over the total kinetic energy flux, increases under the effect of a stronger magnetic confinement. These propulsive considerations are further confirmed by taking into account the plot of the cumulative magnetic thrust. Figure 6, in fact, shows a noticeable improvement in the magnetic thrust when moving from the mildly magnetized case ($\chi = 3$) to higher magnetizations. Note however, that the imparted magnetic thrust does not scale proportionately with the strength of the magnetic field, and that it appears that already at $\chi = 10$ the maximum magnetic thrust of this MA has almost been reached. A similar scaling of the magnetic thrust with the magnetic field was obtained by Andrews *et al.* in the PIC simulations of a traditional MN.[18] The trade off between the dimension of the magnets that induce the applied MA topology (and therefore of the strength of said magnetic field), and the thrust obtained from the thruster under design should take into account the non-linear dependence between these two values.

Interestingly, the initial slope of all the thrust curves in Figure 6 results identical. This is caused by the BCs applied at the injection surface, as demonstrated by retrieving the axial derivative of F_m by inserting the expression for j_y obtained from Eq. (5) into Eq. (15):

$$\left.\frac{dF_m}{dz}\right|_{z=0} = -\int_0^{L_x} \frac{B_x}{B} \frac{\chi^2}{(1+\chi^2)} e n_0 \frac{d\Phi_0}{dx}\,dx, \tag{16}$$

which yields approximately the same value for $\chi >> 1$. Here we have expressed σ_e as a function of the Hall parameter, and neglected the small contribution of the ion current in the computation of the total out-of-plane current.

Finally, the first row of plots in Figure 9 shows the electron in-plane current densities obtained for $\chi = 3$ and $\chi = 150$. In the former case, the solution of $\tilde{\jmath}_e$ exhibits two current loops leaving the plasma source near its edges, and returning back to the source along its center. The existence of these loops rises the overall value of $\tilde{\jmath}_e$ in this region, but does not contribute to the net electron current delivered by the source into the plume. This structure, which was already present in the $\chi = 30$ simulation case of Figure 5 (albeit much smaller in importance and extent), is explained as follows. First, we remark again that, for sufficiently high values of χ, the strong perpendicular gradients of Φ imposed at the source are successfully propagated downstream along the magnetic lines, with little diffusion or smoothing. However, as B is lowered and χ becomes sufficiently small, the damping of the perpendicular gradients of Φ as we progress from the source
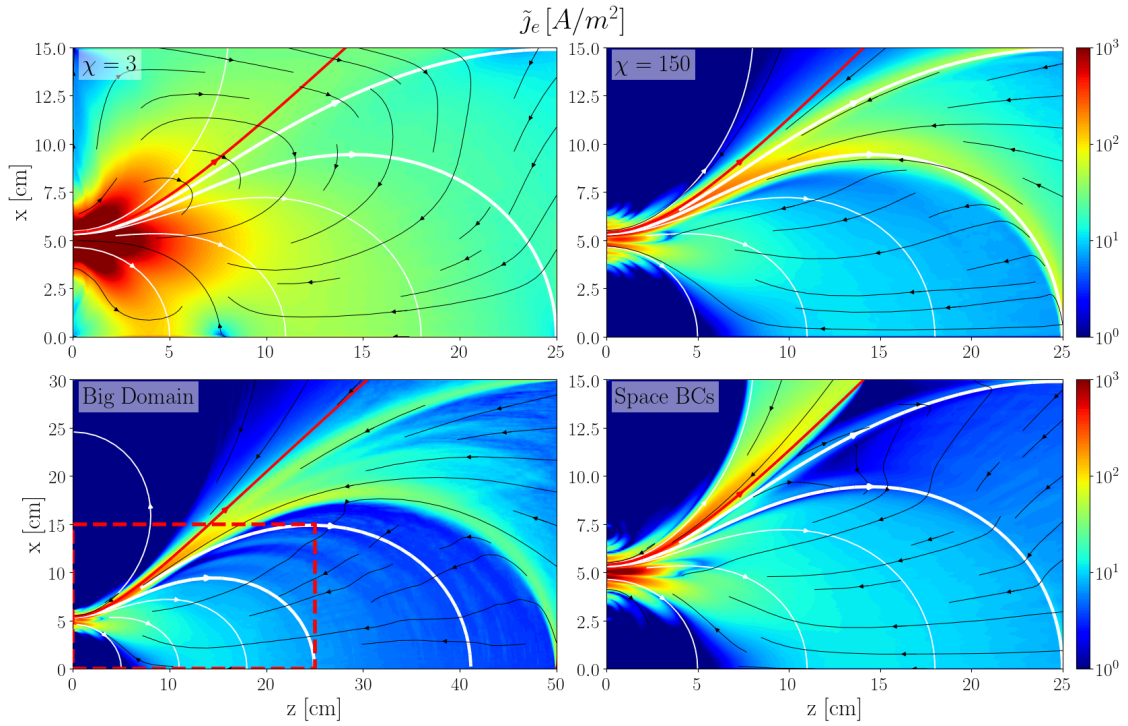
Figure 9: Comparison of the in-plane electron currents for different simulation cases.

and into the domain becomes more marked. Eventually, this mechanism leads to a near-homogeneous value of Φ early in the expansion. Second, this smoothing of the map of Φ means that a non-negligible variation of this quantity takes place along the magnetic lines for small values of χ. We observe that, in the central part of the source exit, the parallel component of $\nabla\Phi$ points upstream, while in the periphery of the source exit it points downstream. Thirdly, since the parallel electron conductivity σ_e is large, the existence of these parallel gradients drives the strong electron currents into and out of the source, respectively. Our numerical experiments prove that this is a robust mechanism present whenever σ_e is sufficiently large, as in this regime Φ results essentially governed by χ alone and is unaffected by σ_e, whereas the parallel electron currents are proportional to the parallel gradient of Φ and σ_e.

Analysing now the rest of the domain in figure 9, it is apparent that for the low magnetization case $\chi = 3$, the electron fluid is well capable of crossing the magnetic lines freely, reaching the outer boundaries without being influenced by the magnetic lines. In the $\chi = 150$ case, instead, the largest portion of the electrons is forced to follow the magnetic tube that reaches the downstream boundaries. The guiding effect of the magnetic lines, already commented for the case with $\chi = 30$, is here further enhanced, causing the streams of current running along the magnetic lines to the domain corners (highlighted once again by the thicker white lines), and the emptying of the semi-circular region above to the symmetry plane, where electrons experience a mobility across the magnetic lines reduced by a factor $\chi^2 + 1$.

VI.   Boundary Effects

It is clear from the plots of the in-plane electron currents described above that, at high values of the Hall parameter, the domain corners and in general the shape and size of the domain affect the solution for $\tilde{\jmath}_e$. If the simulation domain is dictated by the real dimensions of a testing facility then the influence of the domain boundaries on the simulation results is physical: electron currents will preferentially follow those magnetic lines that intersect with the back wall of the vacuum chamber, which may vary for differently shaped and sized facilities. However, if the simulation aims to reproduce the infinite expansion that takes place in space, the BCs imposed at the domain edges should not represent the plasma sheath that develops between the quasi-neutral bulk of the domain and the facility walls, but a global downstream matching layer[40] that connects the domain boundaries to infinity. In this case, therefore, the applied BCs constitute a numerical

scheme that should not influence the simulation results. For this reason we dedicate the present Section to the analysis of the effects that the domain boundaries have on the simulation results.

Firstly, we note that for lower values of the Hall parameter ($\chi = 3$) the chamber boundary conditions employed up to here hold also for an infinite expansion. Indeed, because electrons in this case can freely cross the magnetic lines when expanding to infinity the expression for a global matching layer results analogous to the expansion in a Debye sheath. On the other hand, at higher χ, when the magnetic field has a larger influence in the electrons' motion towards infinity, the choice of appropriate BCs becomes more challenging. In order to assess the effects of the domain boundaries in this case, we repeat the case $\chi = 150$ but with the domain size doubled in both directions. The resulting electron currents are shown in the bottom left Panel of Figure 9, where the dashed red box indicates the original domain size. It is clear that once again the electron currents follow the magnetic tube that intersects the downstream boundary, highlighting a dependency of the currents on the domain size and shape. Indeed, marked differences are evident when comparing the electron currents inside of the dashed red rectangle with those in the top right Panel of Figure 9. In the case of the larger simulation domain, in fact, the extended symmetry plane imposes a null current over a bigger portion of the magnetic lines connected with the injection surface, pushing the electron flux tube to those outer magnetic lines that arch beyond the bottom boundary. As stated, this is to be expected when simulating vacuum chambers of different dimensions, but represents a numerical artefact when attempting to reproduce an expansion to infinity.

The outflow BCs introduced in Reference 13 for the electron fluid represent a possible solution to this problem for the specific case of a MA with large values of χ. As already mentioned, in fact, two categories of field lines may be identified in this magnetic topology: closed lines connecting the two plasma sources through the symmetry plane, and open lines circling back towards their original source in the opposite direction. Assuming perfect magnetization of electrons ($\chi \to \infty$), the zero outflow of current imposed at the symmetry plane causes all closed field lines to carry null electron currents. As a consequence, a condition on the normal electron current $j_{ne} = 0$ (numerically what is imposed is $j_n = j_{ni}$) can be applied on all boundary faces lying on closed filed lines, even those that do not cross the symmetry plane inside of the simulation domain. In order to obtain a current free plume, therefore, all electron current must flow through the boundary crossed by the open field lines. As before, Eq. (13) is therefore used to recover the value of ϕ_W (now representing the potential at infinity) that grants the current free condition, and Eq. (12) yields the Neumann BCs to be applied at the cell faces composing this surface. Note for clarity that the treatment of particles remains unvaried with respect to the previous simulation cases.

The currents obtained with the BCs described above are plotted in the bottom right Panel of Figure 9, where we have also highlighted in red the separatix, the magnetic field line that separates closed magnetic lines (above it) and open ones (below). To aid comparison, this same magnetic line has also been traced in red in all other Panels. Notice how, as we increase the domain size from the top right to the bottom left Panel, the beam of electron current shifts closer to the separatrix. It stands to reason that, if we were to simulate an infinite domain, the electron currents would follow the magnetic lines surrounding the separatrix to reach infinity. Indeed, already with a doubled domain size, it is clear that the electron current density map within the red dashed rectangle approaches the one obtained with the modified BCs.

Finally, extremely marginal variations in all other plasma properties have been noticed when altering the domain size or changing the BCs on the electron currents. This is because, due to the large values of the electron conductivity parallel to the magnetic lines, any small variation of the thermalized potential in this direction will cause relevant changes in the electron currents (see Eq. (5)). As a consequence, the solution to the system of fluid equations is capable of complying to any BC imposed on the electron currents with negligible changes in the map of Φ, and therefore negligible influence on the other plasma properties. In general, in fact, in the case of a collisionless plasma, one has $\sigma_e \to \infty$, forcing the gradients of Φ along the magnetic lines to be identically zero in Eq. 5. This causes the electron currents to be completely decoupled from the rest of the plasma in our drift-diffusion model, since their value becomes inconsequential for the determination of Φ. Although this decoupling between the electron currents and the general plasma response causes numerical challenges in the accurate determination of $\tilde{j}_e$, it also ensures that any inaccuracies in its computation will not relevantly affect the plume's response.

VII.   Conclusions

The in-house, hybrid, planar code EP2PLUS has been employed to simulate the expansion of the plasma produced by two EPTs in a magnetic arch, and to further study the effects linked to variations in the magnetic field strength and to facility conditions. The analysis of the general plasma expansion in a MA allows the identification of three distinct regions: (i) a *near plume*, where the plasma in front of each thruster displays a behaviour analogous to that of more traditional MN topologies, (ii) a *transition region*, where the merging of the two distinct plasma beams takes place, and (iii) a *far plume*, in which the lateral profiles of the plume's properties become single peaked, and the distinct plasma beams have fully merged. In particular, a detailed study of the *transition region* unveils the complex kinetics of ions, characterized in this area by a double peaked VDF, and the presence of a region of magnetic drag, due to the closed magnetic lines that arch between the two EPTs, that mildly reduces the total provided magnetic thrust.

A parametric sweep on the strength of the applied magnetic field shows that only small changes are visible for values of the Hall parameter $\chi \geq 10$ both in the general plasma properties and in the propulsive performance of the MA. The only quantities that show a relevant sensitivity to χ in this magnetized regime are the out-of-plane electron currents, which decrease as the Hall parameter increases in order to maintain a roughly constant magnetic force density in the plume, and the in-plane currents, which result decoupled from the other plasma properties for the weakly collisional plasma analyzed, and progressively result constrained to the the magnetic lines that intersect the domain's outflow boundaries as the magnetization level rises. At lower values of χ, instead, the confining effect of the magnetic field begins to break down, and the plasma is capable of diffusing across the magnetic lines, increasing the plume's divergence and reducing the magnetic thrust provided by the MA.

Finally, a further study of boundary effects demonstrates that different domain sizes (corresponding to different dimensions of the experimental facility) impose different electron current paths in a strongly magnetized plasma, although this does not appreciably alter the other plasma properties of the plume. In light of this dependency of the in-plane electron currents on the domain size, we also adopt and test an alternative set of boundary conditions,[13] more suitable for the simulation of the infinite expansion that takes place in space.

References

[1] Eduardo Ahedo. Plasmas for space propulsion. *Plasma Physics and Controlled Fusion*, 53(12):124037, 2011.

[2] Stéphane Mazouffre. Electric propulsion for satellites and spacecraft: established technologies and novel approaches. *Plasma Sources Science and Technology*, 25(3):033002, 2016.

[3] M. Manente, F. Trezzolani, M. Magarotto, E. Fantino, A. Selmo, N. Bellomo, E. Toson, and D. Pavarin. Regulus: A propulsion platform to boost small satellite missions. *Acta Astronautica*, 157:241–249, 2019.

[4] K. Takahashi. Helicon–type radiofrequency plasma thrusters and magnetic plasma nozzles. *Reviews of Modern Plasma Physics*, 3:3, 2019.

[5] S. Pottinger, V. Lappas, C. Charles, and R. Boswell. Performance characterization of a helicon double layer thruster using direct thrust measurements. *Journal of Physics D: Applied Physics*, 44(23):235201, 2011.

[6] J.C. Sercel. Electron-cyclotron-resonance (ECR) plasma thruster research. In *24th Joint Propulsion Conference*, page 2916, 1988.

[7] F. Cannat, T. Lafleur, J. Jarrige, P. Chabert, P.Q. Elias, and D. Packan. Optimization of a coaxial electron cyclotron resonance plasma thruster with an analytical model. *Physics of Plasmas*, 22(5):053503, 2015.

[8] A. Sánchez-Villar, J. Zhou, M. Merino, and E. Ahedo. Coupled plasma transport and electromagnetic wave simulation of an ECR thruster. *Plasma Sources Science and Technology*, 30(4):045005, 2021.

[9] Eduardo Ahedo and Mario Merino. Two-dimensional supersonic plasma acceleration in a magnetic nozzle. *Physics of Plasmas*, 17(7):073501, 2010.

[10] Mario Merino and Eduardo Ahedo. Plasma detachment in a propulsive magnetic nozzle via ion demagnetization. *Plasma Sources Science and Technology*, 23(3):032001, 2014.

[11] A Fruchtman, K Takahashi, C Charles, and RW Boswell. A magnetic nozzle calculation of the force on a plasma. *Physics of Plasmas (1994-present)*, 19(3):033507, 2012.

[12] B.W. Longmier, E.A. Bering, M.D. Carter, L.D. Cassady, W.J. Chancery, F.R.C. Díaz, T.W. Glover, N. Hershkowitz, A.V. Ilin, G.E. McCaskill, et al. Ambipolar ion acceleration in an expanding magnetic nozzle. *Plasma Sources Science and Technology*, 20:015007, 2011.

[13] Mario Merino, Diego García-Lahuerta, and Eduardo Ahedo. Plasma acceleration in a magnetic arch. *Plasma Sources Science and Technology*, 32(6):065005, jun 2023.

[14] S. Di Fede, M. Manente, P.J. Comunian, and M. Magarotto. Magnetic nozzle performance in a cluster of helicon plasma thrusters. *(accepted for publication)*, (June):1–21, 2023.

[15]Célian Boyé, Jaume Navarro-Cavallé, and Mario Merino-Martinez. Preliminary analysis of the magnetic arch plasma expansion in a cluster of two ECR plasma thrusters. In *10th EUCASS Conference*, Lausanne, Switzerland, July 9–13, 2023.

[16]Keon Vereen, John Correy, Hans Martin, Kaito Durkee, Andrew Kullman, Simon Fraser, and Robert M Winglee. Recent advances in the clustering of high power helicon thrusters. In *AIAA Propulsion and Energy 2019 Forum*, page 3902, 2019.

[17]Mario Merino. Motor espacial de plasma sin electrodos con geometría en U, 2019. PCT patent, Spanish Patent Office, Patent no. ES2733773.

[18]Shaun Andrews, Simone Di Fede, and Mirko Magarotto. Fully kinetic model of plasma expansion in a magnetic nozzle. *Plasma Sources Science and Technology*, 2022.

[19]Alberto Marín-Cebrián, Enrique Bello-Benítez, Adrián Domínguez-Vázquez, and Eduardo Ahedo. Non-maxwellian electron effects on the macroscopic response of a hall thruster discharge from an axial–radial kinetic model. *Plasma Sources Science and Technology*, 33(2):025008, feb 2024.

[20]M. Nakles, L. Brieda, G. Reed, W. Hargus, and R. Spicer. Experimental and numerical examination of the BHT-200 Hall thruster plume. In *43rd AIAA/ASME/SAE/ASEE Joint Propulsion Conference & Exhibit*, page 5305, Washington DC, 2007. American Institute of Aeronautics and Astronautics, Reston, VA.

[21]B Wachs and B Jorns. Background pressure effects on ion dynamics in a low-power magnetic nozzle thruster. *Plasma Sources Science and Technology*, 29(4):045002, 2020.

[22]Benjamin Wachs and Benjamin Jorns. Background pressure effects on ion dynamics in a low-power magnetic nozzle thruster. *Plasma Sources Science and Technology*, 29(4):045002, 2020.

[23]Natalie RS Caruso and Mitchell LR Walker. Neutral ingestion effects on plume properties of a radio-frequency plasma discharge. *Journal of Propulsion and Power*, 34(1):58–65, 2018.

[24]Eduardo Ahedo and Mario Merino. On plasma detachment in propulsive magnetic nozzles. *Physics of Plasmas*, 18(5):053504, 2011.

[25]S Baldinucci, Sophia Bergmann, Jack A Hondagneu, Benjamin Wachs, and Benjamin A Jorns. Impact of facility electrical boundary conditions on the performance of an electron cyclotron resonance magnetic nozzle thruster. In *37th International Electric Propulsion Conference*, 2022.

[26]V. Désangles and J. Jarrige D. Packan. Ecra thruster advances, 30w and 200w prototypes latest performances. In *IEPC 2022, Boston*, IEPC-2022-513, 2022.

[27]Filippo Cichocki, Adrián Domínguez-Vázquez, Mario Merino, and Eduardo Ahedo. Hybrid 3D model for the interaction of plasma thruster plumes with nearby objects. *Plasma Sources Science and Technology*, 26(12):125008, 2017.

[28]Filippo Cichocki, Adrián Domínguez-Vázquez, Mario Merino, and Eduardo Ahedo. 3D simulations of a magnetized Hall Effect thruster plume. In *36th International Electric Propulsion Conference*, number IEPC-2019-460, Vienna, Austria, 2019. Electric Rocket Propulsion Society.

[29]Alberto Modesti, Filippo Cichocki, and Eduardo Ahedo. Numerical treatment of a magnetized electron fluid model in a 3d simulator of plasma thruster plumes. *Frontiers in Physics*, 11, 2023.

[30]F. Cichocki, A. Domínguez-Vázquez, M. Merino, P. Fajardo, and E. Ahedo. Three-dimensional neutralizer effects on a Hall-effect thruster near plume. *Acta Astronautica*, 187:498–510, 2021.

[31]Filippo Cichocki, Jaume Navarro-Cavallé, Alberto Modesti, and Gonzalo Ramírez Vázquez. Magnetic nozzle and rpa simulations vs. experiments for a helicon plasma thruster plume. *Frontiers in Physics*, 10, 2022.

[32]R.W. Hockney and J.W. Eastwood. *Computer simulation using particles*. CRC Press, Boca Ratón, FL, 1988.

[33]C.K. Birdsall and D. Fuss. Clouds-in-clouds, clouds-in-cells physics for many-body plasma simulation. *Journal of Computational Physics*, 135(2):141–148, 1997.

[34]E. Ahedo. Using electron fluid models to analyze plasma thruster discharges. *Journal of Electric Propulsion*, 2(1):2, 2023.

[35]Jiewei Zhou. *Modeling and simulation of the plasma discharge in a radiofrequency thruster*. PhD thesis, Universidad Carlos III de Madrid, Leganés, Spain, 2021.

[36]Gabriel Giono, Jón Gudmundsson, Nickolay Ivchenko, Stephane Mazouffre, Käthe Dannenmayer, Lara Popelier, Dimitry Loubere, Mario Merino, and Georgi Olentsenko. Non-maxwellian electron energy probability functions in the plume of a SPT-100 Hall thruster. *Plasma Sources Science and Technology*, 27(1):015006, 2018.

[37]Mario Merino, Pablo Fajardo, Gabriel Giono, Jon Tomas Gudmundsson, Nickolay Ivchenko, Stéphane Mazouffre, Dimitry Loubere, and Käthe Dannenmayer. Collisionless electron cooling in a plasma thruster plume: experimental validation of a kinetic model. *Plasma Sources Science and Technology*, 29(3):035029, 2020.

[38]G.A. Bird. *Molecular Gas Dynamics and the Direct Simulation of Gas Flows*. The Oxford Engineering Science Series. Oxford University Press, Oxford, UK, 1994.

[39]K.U. Riemann. The bohm criterion and sheath formation. *J. Phys. D: Appl. Phys.*, 24:492–518, 1991.

[40]Adrián Domínguez-Vázquez, Jiewei Zhou, Alejandro Sevillano-González, Pablo Fajardo, and Eduardo Ahedo. Analysis of the electron downstream boundary conditions in a 2D hybrid code for Hall thrusters. In *37th International Electric Propulsion Conference*, number IEPC-2022-338, Boston, MA, June 19-23, 2022. Electric Rocket Propulsion Society.